Article

Surface-Enhanced Raman Scattering Activity of ZrO$_2$ Nanoparticles: Effect of Tetragonal and Monoclinic Phases

Mingyue Yi [1], Yu Zhang [1], Jiawen Xu [1], Dingyuan Deng [1], Zhu Mao [2], Xiangchun Meng [1], Xiumin Shi [1,*] and Bing Zhao [3,*]

1   College of Chemical Engineering, Changchun University of Technology, Changchun 130012, China; yimingyue95@163.com (M.Y.); zhangyjy0@163.com (Y.Z.); xujiawen20210719@163.com (J.X.); dengdingyuan0824@163.com (D.D.); mengxiangchun@ccut.edu.cn (X.M.)
2   School of Chemistry and Life Science, Changchun University of Technology, Changchun 130012, China; maozhu@ccut.edu.cn
3   State Kay Laboratory of Supramolecular Structure and Material, Jilin University, Changchun 130012, China
*   Correspondence: shixiumin@ccut.edu.cn (X.S.); zhaob@jlu.edu.cn (B.Z.); Tel.: +86-431-85716463 (X.S.)

Abstract: The effect of the ZrO$_2$ crystal form on surface-enhanced Raman scattering (SERS) activity was studied. The ratio of the tetragonal (T) and monoclinic (M) phases of ZrO$_2$ nanoparticles (ZrO$_2$ NPs) was controlled by regulating the ratio of two types of additives in the hydrothermal synthesis method. The SERS intensity of 4-mercaptobenzoic acid (4–MBA) was gradually enhanced by changing the M and T phase ratio in ZrO$_2$ NPs. The degree of charge transfer (CT) in the enhanced 4–MBA molecule was greater than 0.5, indicating that CT was the main contributor to SERS. The intensity of SERS was strongest when the ratio of the T crystal phase in ZrO$_2$ was 99.7%, and the enhancement factor reached 2.21×10^4. More importantly, the proposed study indicated that the T and M phases of the ZrO$_2$ NPs affected the SERS enhancement. This study provides a new approach for developing high-quality SERS substrates and improving the transmission efficiency of molecular sensors.

Keywords: SERS; ZrO$_2$; M phase; T phase; charge transfer

1. Introduction

After the phenomenon of surface-enhanced Raman scattering (SERS) was first reported in the mid-1970s, it attracted the attention of many scholars. Researchers have published many articles related to SERS [1,2]. As a fairly new spectral detection technology, SERS has been widely used in the fields of chemistry, physics, biology, and medicine because of its high sensitivity, nondestructive detection, molecular fingerprint information, rapid and simple operation, etc. [3–5]. Single molecule SERS was studied by the Kneipp [6] and Nie [7] research groups in 1997, in which the enhancement factor (EF) reached up to 10^{14}. Nowadays, electromagnetic mechanism (EM) and chemical mechanism (CM) are widely used to explain the enhancement mechanisms of SERS [8–10]. Recently, with the evolution of SERS research, SERS substrates have changed from the original precious metals (Au, Ag and Cu) [11–13] and the expensive metals (Pt and Pd) [14,15] to semiconductor materials (ZnO, CuO, TiO$_2$) [16–18]. Semiconductor materials have good optics, electrics, biocompatibility, high stability, and low cost compared to the metal substrates. Therefore, they have greater research potential and application prospects [19].

A key problem in SERS research is the selection of suitable substrates and the optimization of the preparation process. Many studies have reported that zirconium dioxide (ZrO$_2$) has excellent properties, such as high temperature, corrosion, and oxidation resistance, thermal and chemical stability, which ensures it is widely used in the production of artificial teeth, high temperature materials, electronics and bio ceramics [20–22]. Specifically, nano-sized ZrO$_2$ has three types of crystal structure: monoclinic (M), tetragonal (T) and cubic

(C) [23,24], in addition to being an N-type semiconductor. Moreover, nano-ZrO_2 exhibits surface and interface, quantum size, and macroscopic quantum tunneling effects [25]. Due to the small particle size, large specific surface area and incomplete coordination of atoms on the surface, there is an increase in the quantity of active sites on the nano-ZrO_2 surface [26]. The electrons and holes, which are produced by nano-ZrO_2 crystal particles under illumination, have strong reduction and oxidation ability as well as high photoelectric conversion efficiency [27]. The application scope of semiconductor materials is expanding with the development of the semiconductor technique. The use of semiconductor materials as SERS substrates is prevalent; however, to date, only two studies describing the use of ZrO_2 as a SERS substrate have been reported. The crystalline form of nano-ZrO_2 is mainly the M phase [24,28] and the EF can reach 10^3. Nano-ZrO_2 is very suitable as a SERS substrate due to its superior characteristics, and using nano-ZrO_2 expands the range of semiconductor nanomaterials as SERS substrates. Meanwhile, it also leads to new applications of nano-ZrO_2, which lay a foundation for the further research of the high-quality material in the application of nano sensor devices. More suitable preparation techniques of nano-ZrO_2 are developed by improving the preparation process. The internal relationship between the SERS properties of a substrate and its structure is a contentious issue in SERS research.

In this work, nano-ZrO_2 was prepared by hydrothermal synthesis and the SERS of 4-mercaptobenzoic acid (4–MBA) adsorbed on ZrO_2 nanoparticles (NPs) was determined. The different crystal forms of ZrO_2 NPs can be prepared by adding different types of additives in the hydrothermal synthesis. More interestingly, the proportion of the different crystal forms of ZrO_2 NPs can be controlled by regulating the proportion of two types of additives. We found that there is an interdependence between the crystal form of ZrO_2 NPs and the intensity of the SERS signal.

2. Materials and Methods

2.1. Chemicals

Zirconium chloride octahydrate ($ZrOCl_2 \cdot 8H_2O$), 1,2-dichloroethane, and diethanolamine were purchased from Shanghai McLean Biochemistry Co., LTD. (Shanghai, China). Ammonia water (25%) and 4–MBA were purchased from Tianjin Furui Fine Chemical Co., LTD (Tianjin, China) and Sigma-Aldrich International Limited (Shanghai, China). Deionized water was used throughout the experiments. All reagents used were analytical grade and were used as supplied for sample preparation.

2.2. Preparation of ZrO_2 NPs

ZrO_2 NPs were prepared using the hydrothermal synthesis method according to the literature [29]. $ZrOCl_2 \cdot 8H_2O$ (3.9710 g) was added to 12 mL of deionized water and dissolved completely with stirring. Then, ammonia solution (10%) was added to the solution until the pH was approximately 7, and a white precipitate was produced. The precipitate was filtered repeatedly and washed with deionized water. The precipitate was transformed into a homogeneous suspension in deionized water, and the pH was adjusted to 9 with the addition of ammonia solution (5 wt %). The concentration of zirconium ions was then adjusted to 0.6 mol/L. Diethanolamine and 1,2-dichloroethane were utilized as a mixed additive to form the different crystal structures of ZrO_2 NPs. The mixing ratios were 1:0, 4:1, 3:1, 2:1, 1:1, 1:2, 1:3, 1:4 and 0:1, respectively. One of the nine ratios of mixed additives was added to each sample of the suspension. The volume ratio of the additives to the suspension was 1:30. The volume of the suspension was adjusted to 16 mL using deionized water. The reaction solution was then stirred for 40 min and placed in a high-pressure hydrothermal reaction vessel. Nine groups of reactors were heated at 180 °C for 72 h. After the reaction, the synthesized ZrO_2 was filtered, washed several times, and dried at room temperature.

2.3. Adsorption of Probe Molecules for SERS Measurement

ZrO_2 (30 mg) with different T phase ratios was dispersed in 15 mL 4–MBA (1×10^{-3} mol/L) ethanol solution. The configured ZrO_2 suspension was magnetically stirred for 8 h at room temperature. After centrifugation, ethanol and deionized water were used to wash the residue trice, and the surface modification of ZrO_2 NPs was obtained.

2.4. Instrumentation

The crystal structure of all the samples was determined using Rikagu Smartlab X-ray diffraction patterns (Tokyo, Japan), with a scanning angle range of 10°–75°, and a scanning speed of 3°/min. SERS spectra were recorded by a Horiba HR Evolution Raman spectrometer (Paris, France) under 532 nm (or 2.33 eV) excitation. All Raman spectra were calibrated using Si plates. The penetration depth and diameter of the laser spot was approximately 10 and 1.3 μm, respectively. Scanning electron microscopy (SEM) was employed to study the size distribution of ZrO_2 NPs using a JEOL-7610P (Tokyo, Japan). Ultraviolet-visible (UV-Vis) diffuse reflectance spectra (DRS) of the ZrO_2 samples were recorded on a Cary 5000 UV-Vis spectrophotometer (Santa Clara, CA, USA) equipped with an integrating sphere using $BaSO_4$ as a reference.

3. Results and Discussion

3.1. Characterization of ZrO_2 NPs

Previous reports [29,30] describe the preparation of ZrO_2 NPs with different crystal forms using different additives during hydrothermal synthesis. Diethanolamine with its strong chelating ability encourages the formation of T–ZrO_2 crystals, whereas alkyl halide 1,2-dichloroethane encourages the formation of M–ZrO_2 crystals. Figure 1 shows the XRD diagram of ZrO_2 NPs prepared by a hydrothermal method using diethanolamine and 1,2-dichloroethane as a mixed additive, and the mixing ratios are 1:0; 4:1; 3:1; 2:1; 1:1; 1:2, 1:3, 1:4, and 0:1, respectively. As shown in Figure 1, there are obvious differences in the crystal form of nano-ZrO_2 prepared with pure diethanolamine or 1,2-dichloroethane as dispersant. The XRD diffraction curve when using diethanolamine as an additive is shown in Figure 1a, the characteristic Bragg reflections for the T phase: T (101), T (200), T (202) and T (131) (PDF card: 50–1089) are respectively at approximately 2θ = 30.45°, 35.30°, 50.26° and 60.2°. This indicates that the phase of ZrO_2 is basically pure T phase [31]. However, the XRD diffraction curve when using 1,2-dichloroethane as an additive is shown in Figure 1i, the characteristic Bragg reflections for the M phase: M (111) and M (−111) (PDF card: 37-1484) are at approximately 2θ = 28.37° and 31.50°, respectively. This indicates that the ZrO_2 crystal phase is basically pure M. Figure 1b–h are the XRD of ZrO_2 NPs prepared using the diethanolamine and 1,2-dichloroethane mixture, in the mixing ratios stipulated above. We concluded that the intensity of the Bragg reflection of the T phase characteristic in the diffraction line (Figure 1b–h) decreases gradually, whereas the Bragg reflection of the M phase characteristic increases gradually with the decrease diethanolamine and the increase 1,2-dichloroethane. The particle size of ZrO_2 NPs was calculated using the Scherrer formula: $D = k\lambda/(\beta \cos \theta)$ [32] and is approximately 15.5–16.7 nm. The particle size of the ZrO_2 NPs was confirmed using the SEM image (Figure S1 and Table S1) and was consistent with the results from the XRD.
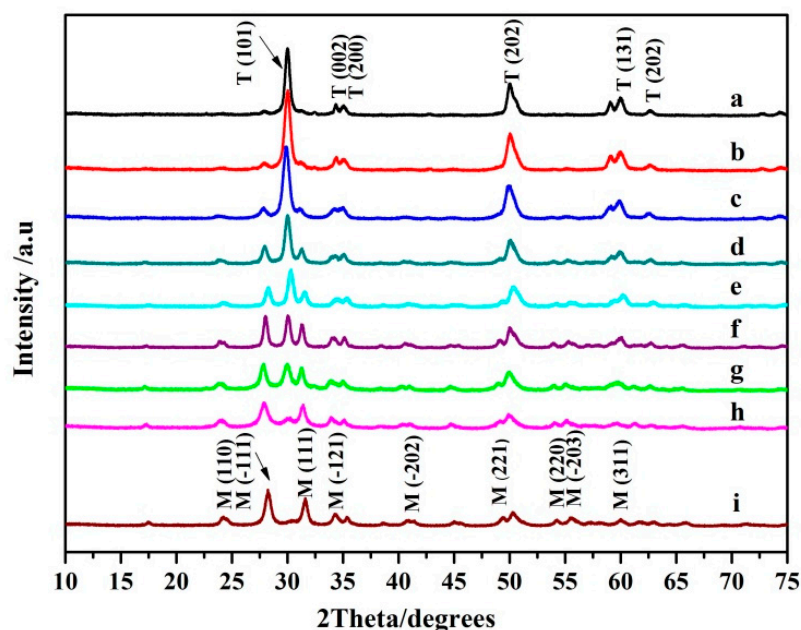
Figure 1. XRD patterns of ZrO$_2$ NPs prepared with different ratios of diethanolamine and 1,2-dichloroethane as mixed additives. (**a–i**) correspond to the mixing ratio of 1:0, 4:1, 3:1, 2:1, 1:1, 1:2, 1:3, 1:4, and 0:1, respectively.

It is necessary to calculate the T phase content in the sample ZrO$_2$. To determine the correlation between the mixing ratio of diethanolamine and 1,2-dichloroethane additives, and the crystal form of the synthesized ZrO$_2$ NPs. The T phase and M phase of ZrO$_2$ can be identified by the most characteristic Bragg reflection of the XRD diffraction lines of all the samples: M ($-$111), T (101) and M (111). There were two M peaks ($-$111) and (111), and one T peak (101) in the sample. The T phase content in ZrO$_2$ was calculated by the relative intensities. First, the strength of the integral of the three Bragg reflections: M ($-$111), T (101), and M (111) of the samples were extracted. Then we calculated the ratio of the T phase using the empirical expressions of Garvie and Nicholson [33,34]. The Formulas (1) and (2) are as follows:

$$X_t \ = \ \frac{I_t(101)}{[I_t(101) + I_m(-111) + I_m(111)]} \tag{1}$$

$$\nu_t \ = \ \frac{1.311X_t}{(1 + 0.311X_t)} \tag{2}$$

where ν_t is the volume fraction of the T phase, X_t is the integrated intensity ratio; I_m (111) and I_m ($-$111) are the (111) and ($-$111) intensities of the M phase of ZrO$_2$, and I_t (101) is the (101) intensity of the T phase of ZrO$_2$, respectively.

The T phase content of the ZrO$_2$ crystal in Figure 1a–i were calculated by Formulas (1) and (2). The ratio of the T phase in the ZrO$_2$ nanoparticles are 99.7%, 81.3%, 70.6%, 63.5%, 41.1%, 29.8%, 19.4%, 11.3%, and 2.5% corresponding to Figure 1a–i, respectively. The results show that ZrO$_2$ with different crystal forms can be synthesized by different types of organic additives in the process of hydrothermal synthesis. The T phase content of ZrO$_2$ NPs can be easily controlled by adjusting the ratio of diethanolamine to 1,2-dichloroethane. The content of the T phase of ZrO$_2$ NPs gradually decreased, with decreasing diethanolamine and increasing 1,2-dichloroethane (Figure 1).

3.2. Raman Spectra of ZrO$_2$ NPs

The Raman spectra of the synthesized ZrO$_2$ NPs are shown in Figure 2. In general, Raman spectra of molecules appear due to the vibrational characteristics of different crystal

phases of ZrO_2. The Raman shifts at less than 800 cm^{-1} were assigned to the ZrO_2 NPs. There were a few distinct vibrational bands located at 145, 266, 313, 458 and 646 cm^{-1} which correspond to the vibrational modes of the T phase of ZrO_2 (Figure 2a). For the T phase of ZrO_2, 6 modes ($1A_{1g} + 3E_g + 2B_{1g}$) are Raman active [35]; the E representations are two dimensional whereas the other modes are one dimensional. This suggests that the ZrO_2 is essentially pure T phase when diethanolamine is used as an additive. However, there were a few distinct vibrational bands located at 177, 188, 328, 338, 378, 475, and 612 cm^{-1} which correspond to the vibrational modes of the M phase of ZrO_2 (Figure 2i). For the M phase of ZrO_2, 18 modes ($9A_g + 9B_g$) are Raman active [36]. This indicates that the ZrO_2 is essentially pure M phase when 1,2-dichloroethane is used as an additive. The curves (b–h) are the Raman spectra of ZrO_2 NPs prepared using diethanolamine and 1,2-dichloroethane as additives, in the stipulated ratios. As shown in Figure 2b–h, the vibrational mode intensity of the T phase of ZrO_2 gradually decreases, whereas the vibration mode of M phase of ZrO_2 gradually increases, with decreasing diethanolamine and increasing 1,2-dichloroethane. This indicates that the results of the Raman and XRD analyses are consistent.
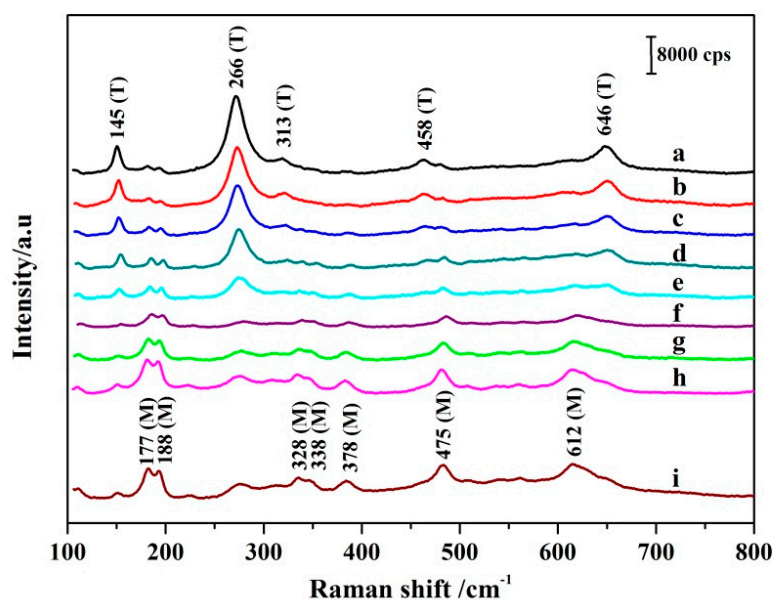
Figure 2. Raman spectra of ZrO_2 NPs prepared with different ratios of diethanolamine and 1,2-dichloroethane as mixed additives. (**a–i**) correspond to the mixing ratio: 1:0, 4:1, 3:1, 2:1, 1:1, 1:2, 1:3, 1:4, and 0:1, respectively.

According to a previous report [37], the proportion of specific crystal forms of molecules can be estimated by using the characteristic bands of different crystal phases in the Raman spectra of molecules. As is illustrated in Figure 2 (curves a and i), the T and M phases of ZrO_2 can be identified by the most representative Raman displacement located at the following positions: T (145, 266, and 646 cm^{-1}) and M (177, 188, and 612 cm^{-1}). The T phase content in ZrO_2 was calculated by the relative intensities of the T bands located at 145, 266, and 646 cm^{-1}, and the M bands located at 177, 188 and 612 cm^{-1}. The ratios of the T phase of ZrO_2 were calculated using the empirical expressions of Clarke and Adar [38]. The formula is as follows (3):

$$\nu_t = \frac{0.97[I_t(145) + I_t(266) + I_t(646)]}{0.97[I_t(145 + I_t(266) + It(646)] + [I_m(177) + I_m(188) + I_m(612)]} \quad (3)$$

where m and t represent the M and T phases, ν_t is the ratio of the T phase of ZrO_2, I_m is the intensity of the M phase of ZrO_2, and I_t is the intensity of the T phase of ZrO_2, respectively. The ratio of the T phase in ZrO_2 NPs is: 99.6%, 82.0%, 70.1%, 63.4%, 41.5%, 29.7%, 19.0%,

11.5%, and 2.6% corresponding to a–i in Figure 2, respectively. These calculation results are in good agreement with those calculated using the characteristic diffraction peaks of XRD.

3.3. UV-Vis DRS Spectra of ZrO$_2$ NPs

The optical properties of ZrO$_2$ NPs were studied by the UV-Vis DRS technique. Figure 3 shows the absorbance spectra of ZrO$_2$ at different crystal ratios. The UV-Vis absorption spectrum of the semiconductor can determine its band gap energy and surface defect state [39]. The strong absorption band of nine samples at less than 250 nm is due to the band-band energy transition of ZrO$_2$ NPs. The trailing absorption bands at 250–430 nm are assigned to the surface defect state of ZrO$_2$. The optical band gap and incident photon energy correspond to the transformed Kubelka–Munk function [40]. The calculated value of the band gap energy (Eg(eV))and the photo-absorption thresholds (λ_g(nm)) can be achieved from the Figure S2 and Table S2 of the Supplementary Information. Thus, the Eg with λ_g of ZrO$_2$ which corresponds to the curves of a–i are 2.96 (419), 3.16 (392), 3.41 (364), 3.66 (339), 3.81 (325), 3.95 (314), 4.22 (294), 4.41 (281), and 4.68 eV (265 nm), respectively [41]. It is noteworthy that with the increase of the T phase ratio in ZrO$_2$, the λ_g of band-band Transition for ZrO$_2$ are red shifted, and the intensity of the tail absorption band at 250–430 nm is gradually enhanced. The greater the red shift of the optical absorption threshold, the higher the threshold, the smaller its band gap energy. The greater the strength of the trailing absorption bands indicates the stronger the surface defect strength. When the ratio of the T crystal phase in ZrO$_2$ is the greatest, the absorbance bands assigned to the ZrO$_2$ have the largest red shift and the strongest strength of the trailing absorption band, thus indicating that it has the best abundant surface properties. The smaller the band gap energy and the better abundant surface defect state of the semiconductor, the more favorable the electron transfer.
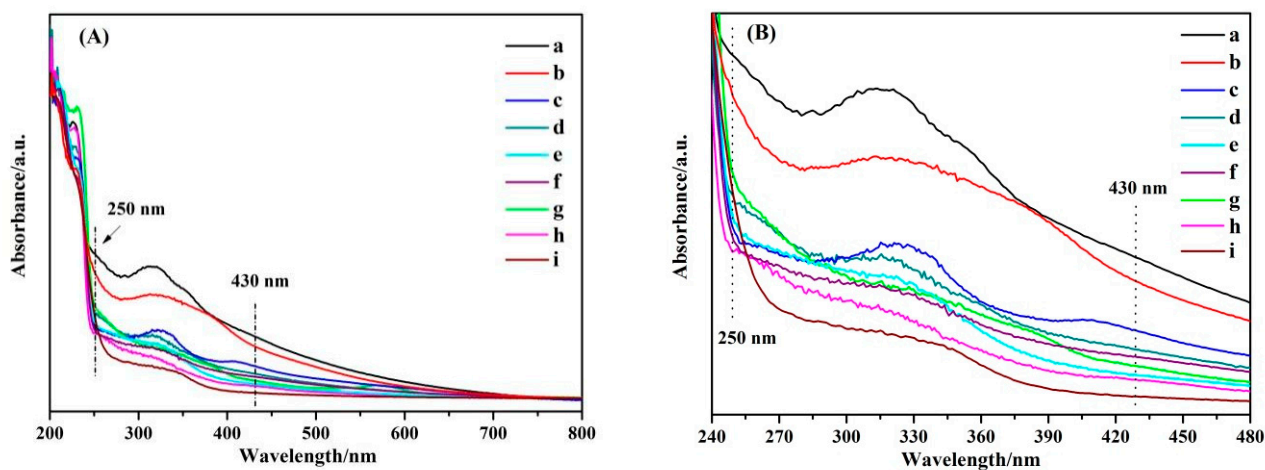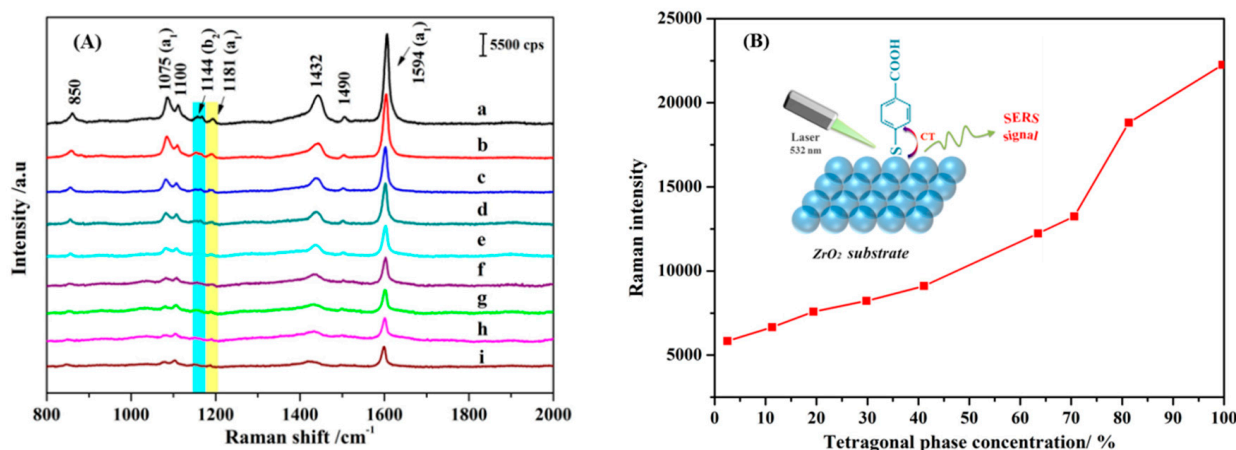

Figure 3. (**A**) UV-Vis DRS spectra of ZrO$_2$ NPs with different T phase proportions; (**B**) UV-Vis DRS spectra of ZrO$_2$ NPs with different T phase proportions in the range 240–480 nm.

3.4. Crystal Form-Dependence of SERS

Generally, ZrO$_2$ have M, T, and C crystal forms, and the different crystal forms have different grain boundary structures. However, the structure of the grain boundary will affect the electrical and optical properties of ZrO$_2$. To examine the effect of the crystal form of ZrO$_2$ on the SERS, Figure 4A shows the SERS spectra of 4–MBA adsorbed on ZrO$_2$ NPs with different T phase proportions. Notably, as the T phase ratio increases and the M phase ratio decreases, the SERS signal of 4–MBA adsorbed on the ZrO$_2$ NPs gradually increases. When the ratio of the T phase in ZrO$_2$ NPs is close to that of the pure T phase, the SERS signal is at maximum. When the ratio of the M phase in ZrO$_2$ NPs is close to that of the pure M phase, the SERS intensity decreases significantly. The strongest Raman intensity was obtained from the pure T phase, which is approximately four times that of the pure M

phase (Figure 4B). Thus, the interdependency between the form of the crystalline phase in ZrO_2 NPs and the SERS enhancement effect can be confirmed. The T phase of ZrO_2 favors CT in the SERS enhancement more than the M phase. This is because of the effect of the grain boundary structure of the different crystalline phases on the electrical and optical properties of ZrO_2. In addition, the T crystalline phase of ZrO_2 has more abundant surface states, which is more conducive to the occurrence of CT.

Figure 4. (**A**) SERS spectra of 4–MBA adsorbed on ZrO_2 NPs with different T phase proportions. (**B**) The relationship between SERS intensities of 4–MBA at the 1594 cm^{-1} mode and the T phase concentration in ZrO_2 NPs.

3.5. Evaluation of EF

To evaluate the SERS activity of ZrO_2 NPs, EF was employed to reflect the enhancement ability. To accurately calculate the values of EF, the Raman spectra of 4–MBA adsorbed on ZrO_2 NPs, and of the solid 4–MBA powders were obtained as shown in Figure 5. The calculation method adopts Formula (4) [42]:

$$EF = \frac{I_{Surf}}{I_{Bulk}} \times \frac{N_{Bulk}}{N_{Surf}} \qquad (4)$$

where I_{surf} and I_{Bulk} represent the SERS intensity of 4–MBA adsorbed on the ZrO_2 NPs and 4–MBA solid powders at 1594 cm^{-1} (assigned to the characteristic vibration of the ν(C–C) aromatic ring), respectively. N_{Surf} and N_{Bulk} represent the number of molecules adsorbed on ZrO_2 NPs and 4–MBA solid powders, respectively.

The value of I_{surf}/I_{Bulk} is equal to the Raman intensity ratio of the 4–MBA@ZrO_2 to the bulk 4–MBA in Figure 5, and the calculated result is 1.8. N_{Bulk} (the number of bulk 4–MBA detected in the 1.3 μm laser spot) was estimated to be 7.61×10^{10} based on 532 nm laser excitation, the focusing penetration depth of the laser (~10 μm), and the density of the 4–MBA (1.5 g·cm^{-3}) [43]. If the ZrO_2 NPs are assumed to be uniformly distributed in a single layer, and the boundary density of 4–MBA adsorbed on the NPs surface is 0.5 nmol/cm^2, the calculated N_{Surf} is 6.146×10^6 [43]. The results of the above calculation are substituted into Formula (4), and the value of EF is 2.21×10^4.
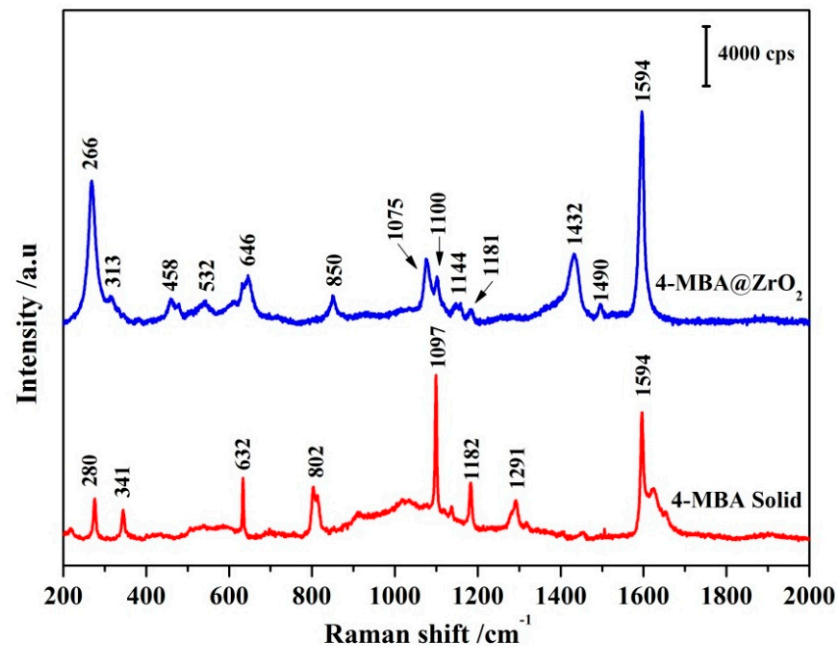
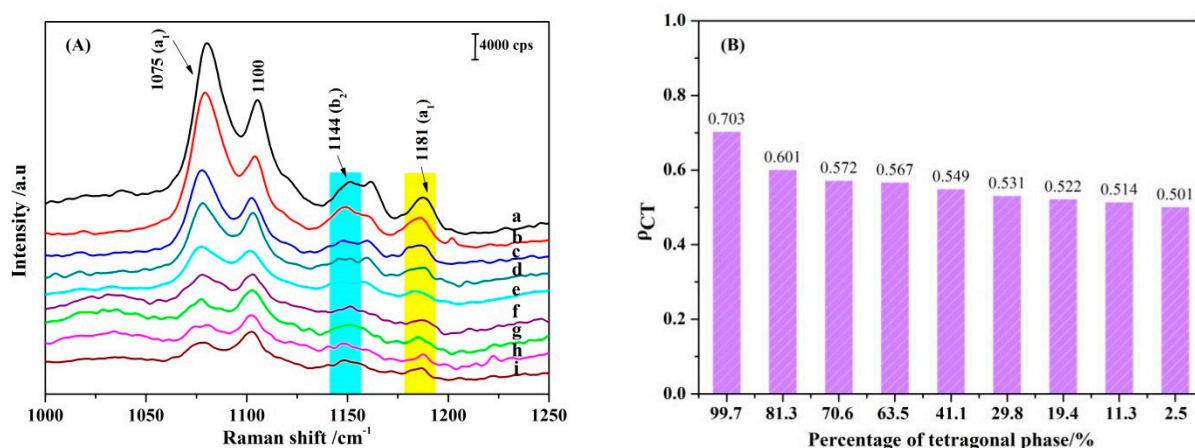**Figure 5.** SERS spectra of 4–MBA adsorbed on ZrO$_2$ NPs and Raman spectra of the 4–MBA bulk sample.

3.6. Degree of Charge Transfer

CT is also the major contribution to SERS in addition to surface plasmon resonance (SPR) and molecular transition [44]. In accordance with previous reports, we employed the degree of CT ($\varrho_{CT}(k)$) to measure the CT contribution to SERS. The concept of $\varrho_{CT}(k)$ can be defined by the following Formula (5) [45]:

$$\varrho CT(k) = \frac{I^k(CT) - I^k(SPR)}{I^k(CT) + I^0(SPR)} \tag{5}$$

where k refers to a specific band in the Raman spectrum. In this equation, $I^k(CT)$ and $I^k(SPR)$ are the intensities of the k band in the presence of CT and EM contribution, respectively, whereas $I^0(SPR)$ is the intensity of the fully symmetric vibrational mode, selected in the spectral region with only SPR contribution. k can be a fully symmetric or non-fully symmetric line. For a fully symmetric line, $I^k(SPR) = I^0(SPR)$, but in the latter, $I^k(SPR)$ is usually quite small [46,47], and we can think of it as being negligible, that is, $I^k(SPR) = 0$. It can be seen from Formula (5) that when $\varrho_{CT} = 0$, there is no CT contribution, and when $\varrho_{CT} = 1$, the intensity of SERS mainly comes from the CT effect. When $\varrho_{CT} = 1/2$, the contribution of CT and EM is equal. As shown from Figure 6A, because the peak at 1144 cm^{-1} is an independent b$_2$ vibrational mode, it is selected as the research object of CT contribution, that is, I^k(CT). The frequency band at 1181 cm^{-1} is an independent a$_1$ vibrational mode, which is selected as I^0(SPR). After selecting the contribution peaks of the corresponding objects, the relationship of ϱ_{CT} and the ZrO$_2$ NPs with different T phases were shown in Figure 6B. The ϱ_{CT} value indicates that when the ratio of diethanolamine to 1,2-dichloroethane is 1:0, and the purity of T zirconia is 99.7%, the CT degree is the strongest. With a decrease in purity, the CT degree gradually decreases, and all of them are greater than 0.5, indicating that CT is the main contributor to SERS intensity.
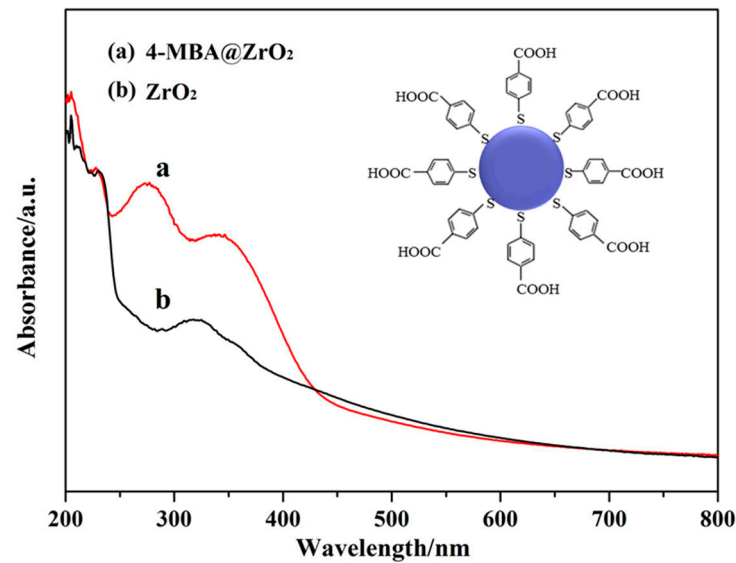
Figure 6. (**A**) SERS spectra of 4–MBA adsorbed on ZrO$_2$ NPs with different T phase proportions. (**B**) Degree of charge transfer (ϱ_{CT}) values of the different T phase proportions of ZrO$_2$ NPs based on 532 nm laser excitation.

3.7. SERS Mechanisms of ZrO$_2$ NPs

The enhancement mechanism of SERS has always been a core contentious issue in the research of SERS substrate development. The study of the SERS enhancement mechanism provides theoretical guidance for the development of high-quality SERS substrates. There are two widely accepted SERS mechanisms to expound the SERS influence. One is EM and the other is CM. The EM effect is due to the local electric field generated by the collective oscillation of the plasma on the metal surface [48,49]. The CM effect is because the CT process between the substrate and the molecule can induce CM. The CT processes typically occur between metal or semiconductor substrates, and the probe molecules. As the SPR is some distance away from the visible region, the SERS effect of most semiconductor materials is due to the CT between semiconductor materials and molecules. As shown in 4–MBA@ZrO$_2$ of Figure 5, the Raman spectra of 4–MBA on ZrO$_2$ are similar to those of 4–MBA on other semiconductor materials reported in the literature. Two stronger Raman bands at 1075 and 1594 cm^{-1} are attributed to the ν_{12} (a$_1$) and ν_{8a} (a$_1$) modes of the respiratory vibration in the aromatic ring, respectively. The other two weaker Raman bands at 1144 and 1181 cm^{-1} are assigned to the ν_{15} (b$_2$) and ν_9 (a$_1$) [50,51] modes of the bending deformation vibration, respectively.

In contrast, it can be seen from the comparison of the UV absorption spectra of ZrO$_2$ and 4–MBA@ZrO$_2$ (Figure 7), that after 4–MBA adsorption, the intensity of the band energy transition absorption band of ZrO$_2$, at less than 250 nm, has increased, and the red shift is significant. At 250–430 nm, the increase in the tail band intensity was greater and the degree of the red shift was larger than that at 250 nm. These changes indicate a CT process between the 4–MBA and the ZrO$_2$ NPs [52]. The obvious changes in the tail band intensity and the degree of the red shift of the bands at 250–430 nm indicated that the surface state energy level, caused by surface defects, plays an important role in the CT process. The degree of surface defects directly affects the CT process and eventually leads to the SERS effect. Similar results were found in the Cu$_2$O–4–MBA system [53].

Figure 7. UV-Vis DRS spectra of (**a**) 4–MBA adsorbed on the ZrO_2 NPs and (**b**) ZrO_2 NPs (the ratio of T phase is 99.7%). The inset is the schematic diagram of 4–MBA adsorbed on ZrO_2 NPs.

The CT process in the SERS system of a semiconductor-molecule depends on the vibration coupling between the semiconductor and molecular energy levels. The direction of CT relies on the energy levels of the valence (VB) and conduction bands (CB) of the semiconductor, relative to the highest occupied molecular orbitals (HOMO), and the lowest unoccupied molecular orbitals (LUMO) of the adsorbed molecules. The HOMO and LUMO of the adsorption molecule 4–MBA were −8.48 and −3.85 eV, based on previous literature [54,55]. The VB of ZrO_2 is located at −7.6 eV [56]. As the band gap energy of ZrO_2 is 2.96 eV, the calculated CB of ZrO_2 is located at −4.64 eV, (Figure 8). As ZrO_2 with a large amount of oxygen vacancies enriching the surface states, there are transition energy levels (surface energy levels) between the VB and CB of ZrO_2. A possible CT transfer pattern is shown in Figure 8; incident light of 532 nm (2.33 eV) excites electrons from the VB of the ZrO_2 through the surface state (Ess) energy level to the CB of ZrO_2, then transits to the LUMO of the 4–MBA, and finally radiates out the Raman photons. The surface defects can be explained by using the UV-Vis DRS spectra. It can be seen from the curve i–a in the Figure 3 that with the increase of the T phase ratio in ZrO_2, the intensity of the tail absorption band at 250–430 nm is gradually enhanced, indicating that the degree of surface defect state gradually increases. The rich surface defect state is more beneficial to the SERS effect during CT transfer. With the increase of the T crystal form ratio, more surface defects are produced, which lead to the stronger SERS effect. The experimental results are consistent with the above enhancement mechanism, which indicates that the SERS effect of the ZrO_2 substrate can be improved by adjusting the ratio of the T crystalline phase in the ZrO_2.
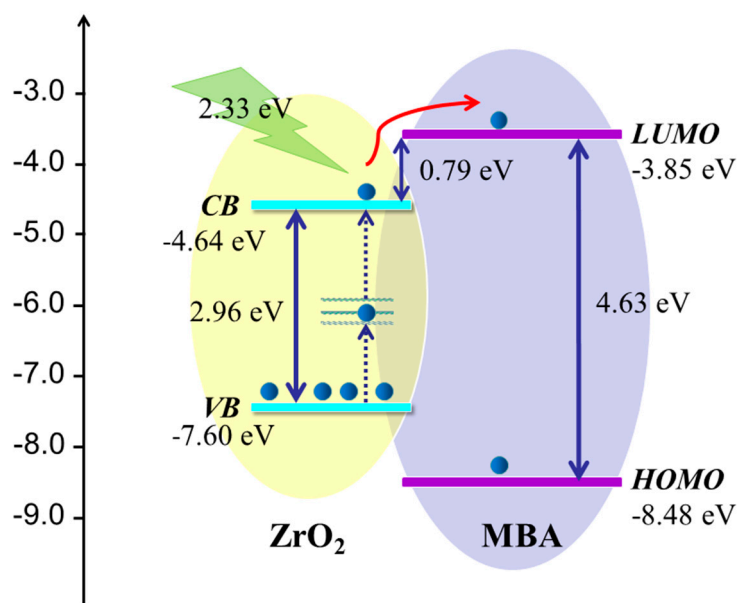
Figure 8. Diagram of the CT mechanism of 4–MBA–ZrO$_2$ system.

4. Conclusions

ZrO$_2$ NPs with different ratios of the crystalline phase were synthesized by hydrothermal synthesis and adjusting the ratio of two additives. The additive, diethanolamine, encourages the formation of T–ZrO$_2$ crystals, whereas 1,2-dichloroethane encourages the formation of M–ZrO$_2$ crystals. The ratio of the T and M phases of ZrO$_2$ NPs can be easily controlled. When the probe molecules of 4–MBA are adsorbed onto the ZrO$_2$, the SERS intensity of 4–MBA is gradually enhanced with the increasing proportion of the T phase of ZrO$_2$ NPs. The strongest SERS intensity of 4–MBA can be obtained by using the pure T phase. The value of EF reached 2.21×10^4. The UV-Vis DRS spectra have shown the interrelation between the band gap energy, surface defect state and the proportion of T phase in ZrO$_2$ NPs. As the proportion of T phase in ZrO$_2$ NPs increases, the band gap energy decreases but the degree of surface defects increases gradually. The smaller band gap energy and the richer surface defect states are conducive to CT transfer between ZrO$_2$ NPs and 4–MBA, consequently showing much stronger SERS signal. This is the main reason that the SERS effect of the T–ZrO$_2$ substrate is stronger than that of the M–ZrO$_2$ substrate. The schematic diagram of CT shows the direction of CT and further indicates that the crystal form of ZrO$_2$ NPs is an important factor affecting the CT. The SERS effect of semiconductor substrates was examined from the perspective of the crystal form of semiconductor nanomaterials in an unprecedented attempt. This study illustrates a new way to develop better quality semiconductor substrates and highlights a new method to improve the charge transport rate for the construction of high sensitivity molecular sensors.

Author Contributions: Writing—original draft preparation, M.Y. and Y.Z.; data curation: J.X. and D.D.; methodology, Z.M. and X.M.; writing—review and editing, X.S. and B.Z. All authors have read and agreed to the published version of the manuscript.

Institutional Review Board Statement: Not applicable.

Informed Consent Statement: Not applicable.

Data Availability Statement: Do not have the supporting reported results.

Conflicts of Interest: The authors declare no conflict of interest.

References

1. Zhang, C.; You, T.; Yang, N.; Gao, Y.; Jiang, L.; Yin, P. Hydrophobic paper-based SERS platform for direct-droplet quantitative determination of melamine. *Food Chem.* **2019**, *287*, 363–368. [CrossRef]
2. Xu, L.J.; Lei, Z.C.; Li, J.; Zong, C.; Yang, C.J.; Ren, B. Label-free Surface-enhanced Raman Spectroscopy Detection of DNA with Single-base Sensitivity. *J. Am. Chem. Soc.* **2015**, *137*, 5149–5154. [CrossRef] [PubMed]
3. Zhang, C.; You, E.; Jin, Q.; Yuan, Y.; Xu, M.; Ding, S.; Yao, J.; Tian, Z. Observing the dynamic "hot spots" on two-dimensional Au nanoparticles monolayer film. *Chem. Commun. (Camb.)* **2017**, *53*, 6788–6791. [CrossRef]
4. Chen, L.; Sa, Y.; Park, Y.; Hwang, H.; Ji, H.; Zhao, B.; Jung, Y.M. Au-MPY/DTNB@SiO$_2$ SERS Nanoprobe for Immunosorbent Assay. *Vib. Spectrosc.* **2016**, *87*, 34–39. [CrossRef]
5. Ji, W.; Song, W.; Tanabe, I.; Wang, Y.; Zhao, B.; Ozaki, Y. Semiconductor-enhanced Raman scattering for highly robust SERS sensing: The case of phosphate analysis. *Chem. Commun. (Camb.)* **2015**, *51*, 7641–7644. [CrossRef] [PubMed]
6. Emory, S.R.; Nie, S. Probing single molecules and single nanoparticles by surface-enhanced raman scattering. *Diss. Indiana Univ.* **1999**, *275*, 1102–1106.
7. Doering, W.E.; Nie, S. Single-Molecule and Single-Nanoparticle SERS: Examining the Roles of Surface Active Sites and Chemical Enhancement. *J. Phys. Chem. B* **2002**, *106*, 311–317. [CrossRef]
8. Kozhina, E.P.; Andreev, S.N.; Tarakanov, V.P.; Bedin, S.A.; Doludenko, I.M.; Naumov, A.V. Study of Local Fields of Dendrite Nanostructures in Hot Spots Formed on SERS-Active Substrates Produced via Template-Assisted Synthesis. *Bull. Russ. Acad. Sci. Phys.* **2020**, *84*, 1465–1468. [CrossRef]
9. Kozhina, E.P.; Bedin, S.A.; Nechaeva, N.L.; Podoynitsyn, S.N.; Tarakanov, V.P.; Andreev, S.N.; Grigoriev, Y.V.; Naumov, A.V. Ag-Nanowire Bundles with Gap Hot Spots Synthesized in Track-Etched Membranes as Effective SERS-Substrates. *Appl. Sci.* **2021**, *11*, 1375. [CrossRef]
10. Fateixa, S.; Nogueira, H.I.; Trindade, T. Hybrid nanostructures for SERS: Materials development and chemical detection. *Phys. Chem. Chem. Phys.* **2015**, *17*, 21046–21071. [CrossRef] [PubMed]
11. Ma, X.; Turasan, H.; Jia, F.; Seo, S.; Wang, Z.; Liu, G.L.; Kokini, J.L. A novel biodegradable ESERS (enhanced SERS) platform with deposition of Au, Ag and Au/Ag nanoparticles on gold coated zein nanophotonic structures for the detection of food analytes. *Vib. Spectrosc.* **2020**, *106*, 103013. [CrossRef]
12. El-Aal, M.A.; Seto, T.; Matsuki, A. The effects of operating parameters on the morphology, and the SERS of Cu NPs prepared by spark discharge deposition. *Appl. Phys. A* **2020**, *126*, 572. [CrossRef]
13. Yu, Z.; Park, Y.; Chen, L.; Zhao, B.; Jung, Y.M.; Cong, Q. Preparation of a Superhydrophobic and Peroxidase-like Activity Array Chip for H$_2$O$_2$ Sensing by Surface-Enhanced Raman Scattering. *ACS Appl. Mater. Interfaces* **2015**, *7*, 23472–23480. [CrossRef] [PubMed]
14. Shin, J.H.; Kim, H.G.; Baek, G.M.; Kim, R.; Jeon, S.; Mun, J.H.; Lee, H.-B.-R.; Jung, Y.S.; Kim, S.O.; Kim, K.N.; et al. Fabrication of 50 nm scale Pt nanostructures by block copolymer (BCP) and its characteristics of surface-enhanced Raman scattering (SERS). *RSC Adv.* **2016**, *6*, 70756–70762. [CrossRef]
15. Kundu, S.; Yi, S.I.; Ma, L.; Chen, Y.; Dai, W.; Sinyukov, A.M.; Liang, H. Morphology Dependent Catalysis and Surface Enhanced Raman Scattering (SERS) Studies using Pd Nanostructures in DNA, CTAB and PVA Scaffolds. *Dalton Trans.* **2017**, *46*, 9678–9691. [CrossRef] [PubMed]
16. Lin, J.; Yu, J.; Akakuru, O.U.; Wang, X.; Yuan, B.; Chen, T.; Guo, L.; Wu, A. Low Temperature-boosted High Efficiency Photo-induced Charge Transfer for Remarkable SERS Activity of ZnO nanosheets. *Chem. Sci.* **2020**, *11*, 9414–9420. [CrossRef] [PubMed]
17. Martinez Nuñez, C.E.; Delgado-Beleño, Y.; Rocha-Rocha, O.; Calderón-Ayala, G.; Florez-López, N.S.; Cortez Valadez, M. Chemical bonding mechanism in SERS effect of pyridine by CuO nanoparticles. *J. Raman Spectrosc.* **2019**, *50*, 1395–1404. [CrossRef]
18. Tanabe, I.; Ozaki, Y. Consistent changes in electronic states and photocatalytic activities of metal (Au, Pd, Pt)-modified TiO$_2$ studied by far-ultraviolet spectroscopy. *Chem. Commun. (Camb.)* **2014**, *50*, 2117–2119. [CrossRef]
19. Han, X.X.; Ji, W.; Zhao, B.; Ozaki, Y. Semiconductor-Enhanced Raman Scattering: Active Nanomaterials and Applications. *Nanoscale* **2017**, *9*, 4847–4861. [CrossRef] [PubMed]
20. Zhao, N.; Pan, D.; Nie, W.; Ji, X. Two-Phase Synthesis of Shape-Controlled Colloidal Zirconia Nanocrystals and Their Characterization. *J. Am. Ceram. Soc.* **2006**, *128*, 10118. [CrossRef] [PubMed]

21. Aati, S.; Akram, Z.; Ngo, H.; Fawzy, A.S. Development of 3D printed resin reinforced with modified ZrO_2 nanoparticles for long-term provisional dental restorations. *Dent. Mater.* **2021**, *37*, e360–e374. [CrossRef]

22. Cao, W.; Kang, J.; Fan, G.; Yang, L.; Li, F. Fabrication of Porous ZrO_2 Nanostructures with Controlled Crystalline Phases and Structures via a Facile and Cost-Effective Hydrothermal Approach. *Ind. Eng. Chem. Res.* **2015**, *54*, 12795–12804. [CrossRef]

23. Gupta, T.K.; Bechtold, J.H.; Kuznicki, R.C.; Cadoff, L.H.; Rossing, B.R. Stabilization of tetragonal phase in polycrystalline zirconia. *J. Mater. Sci.* **1997**, *12*, 2421–2426. [CrossRef]

24. Ji, P.; Mao, Z.; Wang, Z.; Xue, X.; Zhang, Y.; Lv, J.; Shi, X. Improved Surface-Enhanced Raman Scattering Properties of ZrO_2 Nanoparticles by Zn Doping. *Nanomaterials* **2019**, *9*, 983. [CrossRef] [PubMed]

25. Peymani, R.; Poursalehi, R.; Yourdkhani, A. DC Arc discharge synthesized zirconia nanoparticles: Shed light on arc current effects on size, crystal structure, optical properties and formation mechanism. *Mater. Res. Express* **2019**, *6*, 112276. [CrossRef]

26. Liu, Q.; Jiang, L.; Guo, L. Precursor-directed self-assembly of porous ZnO nanosheets as high-performance surface-enhanced Raman scattering substrate. *Small* **2014**, *10*, 48–51. [CrossRef] [PubMed]

27. Ezhil Vilian, A.T.; Chen, S.-M.; Piraman, S. The electrochemical synthesis of Pt particles on ZrO_2–ERGO modified electrodes with high electrocatalytic performance for methanol oxidation. *New J. Chem.* **2015**, *39*, 953–961. [CrossRef]

28. Ji, P.; Wang, Z.; Shang, X.; Zhang, Y.; Liu, Y.; Mao, Z.; Shi, X. Direct Observation of Enhanced Raman Scattering on Nano-Sized ZrO_2 Substrate: Charge-Transfer Contribution. *Front. Chem.* **2019**, *7*, 245. [CrossRef]

29. Jiao, X.; Chen, D.; Xiao, L. Effects of organic additives on hydrothermal zirconia nanocrystallites. *J. Cryst. Growth* **2003**, *258*, 158–162. [CrossRef]

30. Qin, D.; Chen, H. The influence of alcohol additives on the crystallization of ZrO_2 under hydrothermal conditions. *J. Mater. Sci.* **2006**, *41*, 7059–7063. [CrossRef]

31. Heuer, A.H.; Claussen, N.; Kriven, W.M.; Ruhle, M. Stability of Tetragonal ZrO_2 Particles in Ceramic Matrices. *J. Am. Ceram. Soc.* **1982**, *65*, 642–650. [CrossRef]

32. Yang, L.; Jiang, X.; Ruan, W.; Zhao, B.; Xu, W.; Lombardi, J.R. Observation of Enhanced Raman Scattering for Molecules Adsorbed on TiO_2 Nanoparticles: Charge-Transfer Contribution. *J. Phys. Chem. C* **2008**, *112*, 20095–20098. [CrossRef]

33. Toraya, H.; Yoshimura, M.; Somiya, S. Calibration Curve for Quantitative Analysis of the Monoclinic-Tetragonal ZrO_2 System by X-Ray Diffraction. *J. Am. Ceram. Soc.* **2010**, *67*, C-119–C-121.

34. Kim, B.K.; Hahn, J.W.; Han, K.R. Quantitative phase analysis in tetragonal-rich tetragonal/monoclinic two phase zirconia by Raman spectroscopy. *J. Mater. Sci. Lett.* **1997**, *16*, 669–671. [CrossRef]

35. Xu, J.P.; Wang, J.F.; Lin, Y.B.; Liu, X.C.; Lu, Z.L.; Lu, Z.H.; Lv, L.Y.; Zhang, F.M.; Du, Y.W. Effect of annealing ambient on the ferromagnetism of Mn-doped anatase TiO_2 films. *J. Phys. D Appl. Phys.* **2007**, *40*, 4757–4760. [CrossRef]

36. Zhao, X.; Vanderbilt, D. Phonons and lattice dielectric properties of zirconia. *Phys. Rev. B* **2002**, *65*, 075105. [CrossRef]

37. Carlone, C. Raman spectrum of zirconia-hafnia mixed crystals. *Phys. Rev. B Conden. Mat.* **1992**, *45*, 2079–2084. [CrossRef]

38. Duc Huy, L.; Laffez, P.; Daniel, P.; Jouanneaux, A.; The Khoi, N.; Siméone, D. Structure and phase component of ZrO_2 thin films studied by Raman spectroscopy and X-ray diffraction. *Mater. Sci. Eng. B* **2003**, *104*, 163–168. [CrossRef]

39. Yang, L.; Zhang, Y.; Ruan, W.; Zhao, B.; Xu, W.; Lombardic, J.R. Improved surface-enhanced Raman scattering properties of TiO_2 nanoparticles by Zn dopant. *J. Raman Spectrosc.* **2010**, *41*, 721–726.

40. Chang, S.-m.; Doong, R.-a. Interband Transitions in Sol-Gel-Derived ZrO_2 Films under Different Calcination Conditions. *Chem. Mater.* **2007**, *19*, 4804–4810. [CrossRef]

41. Myrick, M.L.; Simcock, M.N.; Baranowski, M.; Brooke, H.; Morgan, S.L.; McCutcheon, J.N. The Kubelka-Munk Diffuse Reflectance Formula Revisited. *Appl. Spectrosc. Rev.* **2011**, *46*, 140–165. [CrossRef]

42. Orendorff, C.J.; Gole, A.; Sau, T.K.; Murphy, C.J. Surface-Enhanced Raman Spectroscopy of Self-Assembled Monolayers: Sandwich Architecture and Nanoparticle Shape Dependence. *Anal. Chem.* **2005**, *77*, 3261–3266. [CrossRef]

43. Jiang, L.; You, T.; Yin, P.; Shang, Y.; Zhang, D.; Guo, L.; Yang, S. Surface-enhanced Raman scattering spectra of adsorbates on Cu_2O nanospheres: Charge-transfer and electromagnetic enhancement. *Nanoscale* **2013**, *5*, 2784–2789. [CrossRef]

44. Richter, A.P.; Lombardi, J.R.; Zhao, B. Size and Wavelength Dependence of the Charge-Transfer Contributions to Surface-Enhanced Raman Spectroscopy in Ag/PATP/ZnO Junctions. *J. Phys. Chem. C* **2010**, *114*, 1610–1614. [CrossRef]

45. Wang, X.; Li, P.; Han, X.X.; Kitahama, Y.; Zhao, B.; Ozaki, Y. Enhanced Degree of Charge Transfer in Dye-sensitized Solar Cells with a ZnO-TiO_2/N3/Ag Structure as Revealed by Surface-enhanced Raman Scattering. *Nanoscale* **2017**, *9*, 15303–15313. [CrossRef]

46. Chu, Q.; Li, J.; Jin, S.; Guo, S.; Park, E.; Wang, J.; Chen, L.; Jung, Y.M. Charge-Transfer Induced by the Oxygen Vacancy Defects in the Ag/MoO_3 Composite System. *Nanomaterials* **2021**, *11*, 1292. [CrossRef]

47. Yang, Y.; Li, J.; Zhang, M.; Song, P.; Lu, X.; Ding, Y. Universal and simple MoO_3 substrate for identification of SERS enhancement mechanism. *J. Raman Spectrosc.* **2021**, *1*, 1–6.

48. Ding, S.-Y.; Yi, J.; Li, J.-F.; Ren, B.; Wu, D.-Y.; Panneerselvam, R.; Tian, Z.-Q. Nanostructure-based plasmon-enhanced Raman spectroscopy for surface analysis of materials. *Nat. Rev. Mater.* **2016**, *1*, 16021. [CrossRef]

49. Xue, X.; Ji, W.; Mao, Z.; Mao, H.; Wang, Y.; Wang, X.; Ruan, W.; Zhao, B.; Lombardi, J.R. Raman Investigation of Nanosized TiO_2: Effect of Crystallite Size and Quantum Confinement. *J. Phys. Chem. C* **2012**, *116*, 8792–8797. [CrossRef]

50. Wang, Y.; Ji, W.; Sui, H.; Kitahama, Y.; Ruan, W.D.; Ozaki, Y.; Zhao, B. Exploring the Effect of Intermolecular H-Bonding: A Study on Charge-Transfer Contribution to Surface-Enhanced Raman Scattering of p-Mercaptobenzoic Acid. *J. Phys. Chem. C* **2014**, *118*, 10191–10197. [CrossRef]
51. Fu, X.; Jiang, T.; Zhao, Q.; Yin, H. Charge-transfer contributions in surface-enhanced Raman scattering from Ag, Ag_2S and Ag_2Se substrates. *J. Raman Spectrosc.* **2012**, *43*, 1191–1195. [CrossRef]
52. Guo, L.; Mao, Z.; Jin, S.; Zhu, L.; Zhao, J.; Zhao, B.; Jung, Y.M. A SERS Study of Charge Transfer Process in Au Nanorod-MBA@Cu_2O Assemblies: Effect of Length to Diameter Ratio of Au Nanorods. *Nanomaterials* **2021**, *11*, 867. [CrossRef]
53. Lin, J.; Hao, W.; Shang, Y.; Wang, X.; Qiu, D.; Ma, G.; Chen, C.; Li, S.; Guo, L. Direct Experimental Observation of Facet-Dependent SERS of Cu_2O Polyhedra. *Small* **2018**, *14*, 1703274. [CrossRef]
54. Lombardi, J.R.; Birke, R.L. Theory of Surface-Enhanced Raman Scattering in Semiconductors. *J. Phys. Chem. C* **2014**, *118*, 11120–11130. [CrossRef]
55. Wang, X.; Shi, W.; She, G.; Mu, L. Surface-Enhanced Raman Scattering (SERS) on transition metal and semiconductor nanostructures. *Phys. Chem. Chem. Phys.* **2012**, *14*, 5891–5901. [CrossRef] [PubMed]
56. Gritsenko, V.; Gritsenko, D.; Shaimeev, S.; Aliev, V.; Nasyrov, K.; Erenburg, S.; Tapilin, V.; Wong, H.; Poon, M.C.; Lee, J.H.; et al. Atomic and electronic structures of amorphous ZrO_2 and HfO_2 films. *Microelectron. Eng.* **2005**, *81*, 524–529. [CrossRef]